https://doi.org/10.5194/egusphere-2026-1395
Preprint. Discussion started: 1 April 2026

An Observational Perspective on Precipitation Efficiency of Mesoscale Convective Systems over the Asian Monsoon Region

Thabo Makgoale[1], Sylvia Sullivan[1,2], and Julia Kukulies[3]

[1]Department of Hydrology and Atmospheric Sciences, University of Arizona, Tucson, Arizona, USA
[2]Department of Chemical & Environmental Engineering, The University of Arizona, Tucson, AZ
[3]Mesoscale and Microscale Meteorology Laboratory, NCAR, Boulder, CO, USA

Correspondence: Thabo Makgoale (temakgoale@arizona.edu) and Sylvia Sullivan (sylvia@arizona.edu)

Abstract. This study investigates the precipitation efficiency (ϵ) of tropical mesoscale convective systems (MCSs) using satellite-based precipitation rates ($\dot{P}$) from GPM IMERG and cloud, ice, and liquid water paths (CWP, IWP, LWP) from the ERA5 reanalysis. We define ϵ as the ratio of $\dot{P}$ to CWP, following Li et al. (2022), and phase-partition it using IWP and LWP. We calculate these metrics for a total of 1321 MCSs tracked by the Python FLEXible Object TRacKeR (PyFLEXTRKR) algorithm and focus on southern Asia during monsoon season, given its frequent MCS occurrence. We first look at spatial distributions, analyzing longitudinal and latitudinal trends in MCS versus non-MCS ϵ. MCS ϵ values are 50% higher than ϵ from non-MCS convection on average and increase more strongly from north to sorth and from west to east. Decompositions of ϵ across different regions of the MCSs indicate that the highest ϵ consistently occurs within the core, followed by the cold and then warm anvils. By scaling ϵ by MCS area and cloud depth, we find that all ϵ metrics increase with area up to an MCS effective diameter of 160 km. This trend is consistent with enhanced ice growth associated with deeper clouds and stronger convective organization in larger MCS, before ϵ decreases again in the largest systems where cloud ice growth has reached its maximum. In contrast, all ϵ metrics increase monotonically with MCS depth, indicating that deeper systems convert cloud condensate into surface precipitation more efficiently without the non-monotonicity observed in the ϵ-area scalings. Finally, ϵ increases rapidly during the first $\sim$20% of the MCS lifecycle and decreases more gradually during the remaining decay phase—consistent with our scalings and reflecting enhanced efficiency during periods of system growth, expansion, and deepening.

1 Introduction

Precipitation efficiency (ϵ) quantifies the effectiveness with which cloud systems convert atmospheric water vapor into condensate and, ultimately, surface precipitation. It encapsulates how quickly cloud processes occur from condensation to rainfall production, thereby linking microphysics to large-scale water and energy budgets. As a consequence, ϵ is a critical process-oriented diagnostic for evaluating the skill of models in predicting precipitation and flash flood potential (e.g., Doswell et al., 1996), elucidating the mechanisms of cloud-radiative feedback (e.g., Sui et al., 2020), and linking cloud diabatic heating structure to large-scale flow (e.g., Tao et al., 2004).

Different types of cloud are characterized by different values of ϵ, due to variations in entrainment, microphysics (e.g., warm-rain versus ice-phase processes), and cloud organization. Recent studies also demonstrate substantial variation in ϵ across

https://doi.org/10.5194/egusphere-2026-1395
Preprint. Discussion started: 1 April 2026

organized systems. For example, tropical cyclones exhibit some of the highest and least variable efficiencies (Kukulies et al., 2026), whereas less organized or weakly aggregated convection tends to produce lower efficiencies, consistent with ongoing debates over how convective organization modulates precipitation intensity (e.g., Bao and Sherwood, 2019; Da-Silva et al., 2021). The response of ϵ across different cloud and weather systems to surface warming remains an open question, further highlighting the importance of understanding ϵ across different cloud types and weather systems. Cloud-resolving simulations in radiative–convective equilibrium indicate that denser clouds with larger condensate amounts, which become more likely with surface warming, convert condensate into precipitation more efficiently (Lutsko and Cronin, 2018). Stronger boundary layer–lower troposphere mixing, by contrast, can reduce the ϵ of low-level liquid clouds and thereby amplify model climate sensitivity (Stevens, 2007). Despite these advances in understanding the driving factors of ϵ, much of the existing literature still emphasizes bulk or domain-averaged estimates of ϵ, and the role of cloud morphology and convective organization in shaping ϵ remains understudied.

Mesoscale convective systems (MCSs) are a form of highly organized cloud system, characterized by deep convective cores and expansive anvil clouds that can cover hundreds of kilometers (Houze, 2004; Liu, 2012). As deep convection aggregates into MCSs, moisture concentrates within active convective regions, while surrounding areas become drier. This spatial organization reduces the entrainment of unsaturated air into convective updrafts, thus limiting the dilution of condensate in the cores (Mauritsen and Stevens, 2015; Wing et al., 2017). Reduced dilution can enhance condensate growth and rainfall production, leading to higher ϵ in strongly organized convection compared to cases with more randomly distributed convection. Consistent with recent studies examining ϵ across storm types (e.g., Kukulies et al., 2026), the protected convective cores of MCSs with strong updrafts can efficiently convert condensate to precipitation, whereas stratiform regions with broader horizontal extent tend to exhibit lower ϵ. The weaker ascent and enhanced mixing of these stratiform regions promote condensate retention and re-evaporation. Understanding MCS ϵ therefore provides a process-oriented pathway to improve precipitation predictions and constrain the representation of convective organization in climate models.

Persistent precipitation biases associated with MCSs have been widely documented in global climate model (GCM) evaluations (e.g., Feng et al., 2021b; Lin et al., 2022; Dong et al., 2023; Hsu et al., 2023). In particular, many GCMs tend to underestimate total MCS rainfall while overestimating extreme precipitation rates, and often fail to reproduce the observed spatial and temporal organization of these systems. A primary cause of these deficiencies is the relatively coarse horizontal grid spacing ($\sim$100 km) and the reliance on parameterized convection in most GCMs, which together inhibit the realistic formation, enhanced growth, and organized propagation of MCSs. As a result, simulated convective systems are typically too localized, intense, and short-lived and lack sufficient stratiform precipitation structure (Dong et al., 2023; Song et al., 2024; Hernández et al., 2025). Increases in computing power have facilitated the development of a new generation of global storm-resolving models (GSRMs), allowing global simulations with horizontal grid spacings of 1 to 5 km that explicitly resolve deep convection without requiring cumulus parameterization. These GSRMs, such as the models participating in the DYnamics of the Atmospheric general circulation Modeled On Non-hydrostatic Domains (DYAMOND) intercomparison (Stevens et al., 2019), therefore offer a powerful means of assessing the processes governing ϵ and its variability across regions dominated by MCSs.

https://doi.org/10.5194/egusphere-2026-1395
Preprint. Discussion started: 1 April 2026

Recent work with GSRM output has shown improvements in simulating frequency, horizontal extent, and diurnal cycle of MCSs compared to parameterized models, in turn yielding improvement in related cloud-radiative feedbacks (Na et al., 2020; Judt and Rios-Berrios, 2021; Ma et al., 2022). However, an overestimate of high-intensity convective rainfall and underestimate of low-intensity stratiform rainfall from MCSs persists within GSRMs, due to poorly resolved mesoscale circulations and microphysical processes (e.g., Han and Hong, 2018; Becker et al., 2021; Zhang et al., 2021). Our recent study examined ϵ in a subset of DYAMOND models and found that the regions where these models strongly over- or underestimate precipitation intensity ($\dot{P}$) relative to satellite data are also the regions dominated by MCS rainfall, particularly the Bay of Bengal, northern Indian Ocean, and the monsoon frontal zone over central India (Makgoale and Sullivan, 2025). We revisit this point in more detail at the start of our results. Because ϵ is defined as the ratio of the surface precipitation rate to the cloud water path, errors in the intensity of rain production or the residence time of condensate within MCSs will directly affect ϵ. ϵ therefore provides a useful evaluation metric, as it constrains not only the simulation of surface rainfall and cloud condensate individually but also their physical coupling, with biases pointing to deficiencies in microphysical conversion processes, condensate retention, or dynamical controls on precipitation formation rather than errors in either field alone.

Both here and in our DYAMOND study, we adopt the ϵ definition proposed by Li et al. (2022), as the ratio of $\dot{P}$ to CWP, for a few reasons. First, ϵ is not dimensionless but is physically interpretable as the inverse of the atmospheric residence time of the condensate. However, we return ϵ in units of h^{-1} because it directly quantifies the rate of condensate-to-precipitation conversion and enables comparison with previous studies. Higher values of ϵ indicate a shorter residence time and a more efficient conversion of condensate to precipitation, while lower values indicate a longer retention of condensate aloft. Second, this formulation is advantageous when using satellite and reanalysis, such as Global Precipitation Measurement (GPM) Integrated MultisatellitE Retrievals (IMERG) and the European Centre for Medium-Range Weather Forecasts Reanalysis v5 (ERA5), as it depends on observable quantities. Lastly, this ϵ definition facilitates model evaluation, as it depends only on two-dimensional model output without requiring computationally expensive microphysical tendencies that are usually not saved as standard model output.

In this study, we investigate the ϵ of tropical MCSs using satellite-based convective tracking and precipitation data and reanalysis-derived cloud water path fields. Our analysis is organized around three primary objectives. First, we evaluate whether systematic geographic differences emerge in ϵ between organized and isolated convective systems, distinguishing contributions of liquid- and ice-phase hydrometeors to rainfall production. Then, we examine how ϵ varies with key structural attributes of MCSs, including their size and vertical extent. Lastly, we quantify the evolution of efficiency over MCS lifecycle from initiation through maturation and decay. By establishing observationally constrained values of ϵ in organized tropical convection, this study aims to advance the physical understanding of MCS precipitation formation processes and provide a basis for evaluating global climate and storm-resolving models.

https://doi.org/10.5194/egusphere-2026-1395
Preprint. Discussion started: 1 April 2026

2 Materials and Methods

2.1 Data Sources

For observational MCS tracking, Feng et al. (2021a) employed precipitation estimates from NASA Global Precipitation Measurement (GPM) Integrated MultisatellitE Retrievals (IMERG V06B; Huffman et al. 2019a) and infrared (IR) brightness temperature (Tb) data from the Global Merged IR product (Janowiak et al., 2017). Both datasets provide a continuous 20-year record that stretches from June 2000 through March 2020. The IMERG data set offers half-hourly surface precipitation rates at $0.1^\circ \times 0.1^\circ$ spatial resolution derived from passive microwave sensors, which were temporally averaged at hourly intervals to ensure consistency during tracking. The IR Tb data, originally available at 4-km spatial resolution and 30-min temporal frequency, were regridded to the $0.1^\circ \times 0.1^\circ$ IMERG grid using the Earth System Modeling Framework (ESMF; ESMPy) bilinear interpolation to enable pixel-level collocation. The resulting Tb precipitation data set provides a globally consistent gridded product on an hourly basis between 60° S and 60° N, allowing a robust evaluation of both the spatial organization and temporal evolution of convective systems throughout their lifecycles.

Cloud condensate data was obtained from the European Centre for Medium-Range Weather Forecasts (ECMWF) ERA5 reanalysis (Hersbach et al., 2020). ERA5 offers hourly global atmospheric fields with 137 vertical levels that extend from the surface to 0.01 hPa and a horizontal resolution of $0.25^\circ \times 0.25^\circ$. The cloud liquid water path (LWP) and cloud ice water path (IWP) are used together with satellite-based $\dot{P}$ estimates. Specifically, LWP is obtained from the ERA5 total column cloud liquid water field, while IWP is constructed as the sum of total column cloud ice water and total column snow water. These column-integrated liquid and frozen condensate fields are summed to yield the total cloud water path (CWP). We note that these ERA5 condensate fields represent 2-D column-integrated grid-scale cloud condensate and do not include frozen hydrometeors produced by the convective parameterization scheme. As a result, ERA5 IWP does not fully represent all frozen condensate associated with deep convective precipitation, particularly convective snowfall. To ensure collocation with satellite-derived precipitation fields, hourly CWP, LWP, and IWP data were interpolated both spatially and temporally to match the GPM IMERG grid data.

Below, we also use the Chalmers Cloud Ice Climatology (CCIC) to evaluate an alternate definition of ϵ. CCIC provides IWP at $0.036^\circ \times 0.036^\circ$ spatial and 30-minute temporal resolution, derived from geostationary infrared satellite observations using a convolutional neural network trained on CloudSat 2C-ICE and 2B-CLDCLASS retrievals. The retrieval relies on 11-μm infrared brightness temperatures from the globally gridded, 3-hourly GridSat-B1 (1980–present) and half-hourly CPCIR (2000–present) datasets. Extensive validation against independent in-situ measurements, spaceborne cloud radar observations, ground-based Cloudnet retrievals, and global cloud ice records demonstrates that CCIC realistically captures the magnitude, spatial structure, and diurnal variability of ice clouds, with correlations of $\sim$0.6 to 0.75 for both IWP and IWC across datasets (Amell et al., 2023; Pfreundschuh et al., 2025).

https://doi.org/10.5194/egusphere-2026-1395
Preprint. Discussion started: 1 April 2026

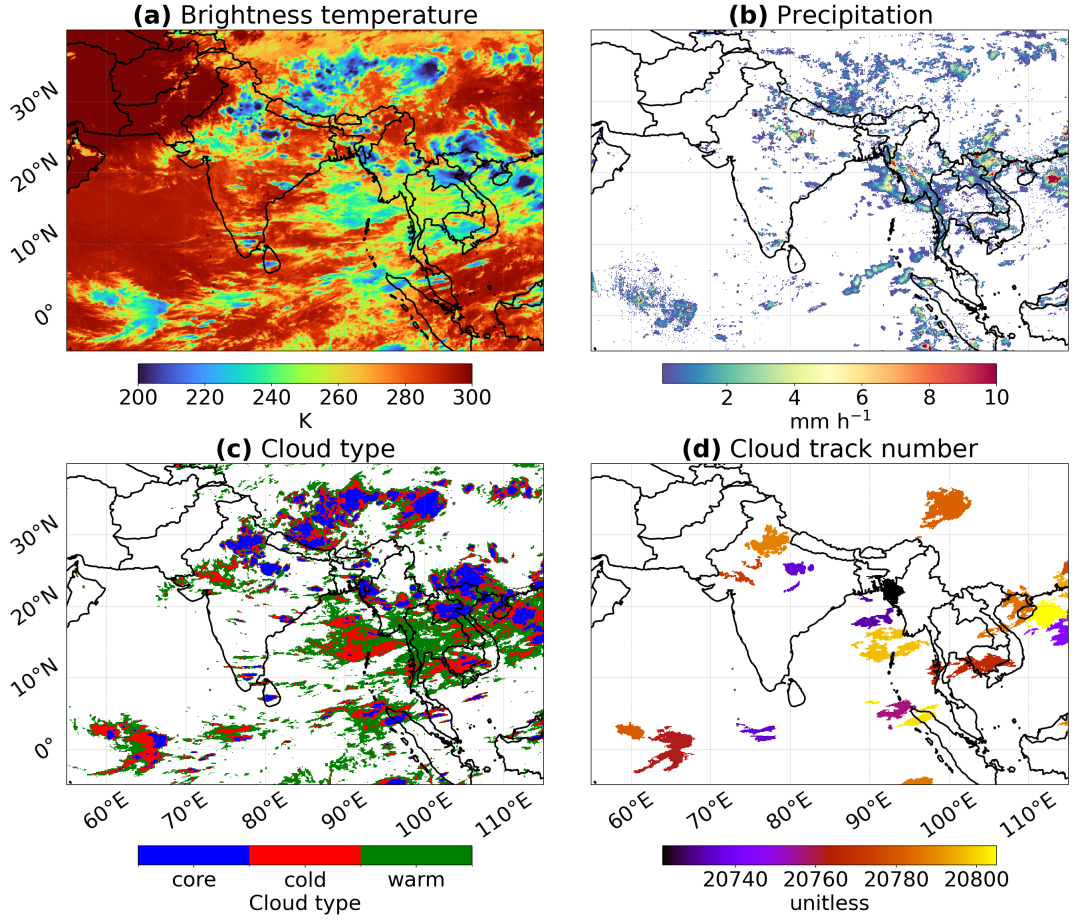

Figure 1. *PyFLEXTRKR brightness temperature and precipitation fields reveal widespread deep convection (Tb < 220 K) with $\dot{P} > 6$ mm h^{-1} over the Asian monsoon region.* Snapshots of pixel-level MCS tracking data on 10 August 2016 over the Asian monsoon region. (a) Brightness temperature [K] highlighting cold cloud tops associated with deep convection, (b) GPM IMERG precipitation [mm h^{-1}] filtered by the pixel-level MCS mask, showing intense rainfall embedded within organized convective systems, (c) Cloud-type classification used by PyFLEXTRKR, distinguishing convective core (blue), cold anvil (red), and warm anvil (green) regions, and (d) Cloud-track numbers assigned by the tracking algorithm, illustrating the spatial extent and segmentation of individual MCSs.

2.2 MCS Tracking Framework

MCSs were identified and tracked using the Python FLEXible Object TRacKeR (PyFLEXTRKR) algorithm (Feng et al., 2018, 2021a). PyFLEXTRKR is an automated feature-tracking framework designed to detect and track the evolution of organized deep convective systems throughout their lifecycles. The MCSs were identified by first detecting a cold cloud core using a Tb threshold of 225 K. From this core, the cold cloud system (CCS) was expanded outward to include neighboring cloud regions with Tb < 241 K, subject to a minimum area of 4×10^4 km^2, using a "detect-and-spread" method to capture

https://doi.org/10.5194/egusphere-2026-1395
Preprint. Discussion started: 1 April 2026

the anvil/outflow region. These cold cloud shields were further refined to MCSs by filtering for those with a collocated precipitation feature (PF) with mean hourly rain rate > 3 mm h^{-1} and a major-axis length exceeding 100 km. PFs were required to meet additional thresholds in area, mean rain rate, rain-rate skewness, and heavy-rain volume ratio, which varied according to the lifetime of the system. Both the CCS and PF criteria had to be satisfied for at least 4 consecutive hours to exclude short-lived convective clusters. Temporal continuity between consecutive time steps was established through centroid overlap and propagation direction, producing time-linked MCS tracks (see Figure 1 in Feng et al. 2021a).

2.2.1 Hourly Pixel Level MCS data

The MCS tracking pixel-level dataset from PyFLEXTRKR exists on a global 0.1° × 0.1° grid at hourly temporal resolution, spanning 60°S to 60°N. Each data file contains spatial fields of Tb, surface precipitation rate, and MCS-masked variables, including track number and core, cold anvil, and warm anvil regions of the MCS. Figure 1a–d provides an example of the PyFLEXTRKR pixel-level data from August 2016 with multiple MCSs observed over the Asian monsoon domain. In the Tb field, colder values (<240 K; blue–green shades) designate deep convective towers and extensive cold anvil clouds embedded within organized systems, while warmer values (>260 K; orange–red shades) represent shallow clouds or cloud-free regions (Figure 1a). In the IMERG precipitation field, localized maxima in $\dot{P}$ of 6–10 mm h^{-1} are collocated with the coldest convective cores (Figure 1b). The PyFLEXTRKR cloud-type classification shows how the convective core (blue) is typically surrounded by cold anvil (red) and warm anvil (green) but with internal heterogeneity between the MCSs (Figure 1c). Lastly, cloud track numbers uniquely label individual MCS objects and enable temporal tracking (Figure 1d). This pixel-level framework facilitates quantification of cloud–precipitation coupling within MCSs and calculation of ϵ at high spatiotemporal resolution.

2.2.2 MCS Track Statistics

In addition to spatial fields, PyFLEXTRKR contains statistics on the structural and evolutionary characteristics of each identified MCS during its lifetime. Each tracked system is assigned a unique identifier, and its properties are temporally aggregated to capture the progression of the convective lifecycle. The dataset includes lifecycle descriptors (e.g., duration of MCS state, start and end epoch time of each track), cloud properties (e.g., area of cold cloud core, area of CCS, and minimum tb in core + cold anvil area), precipitation characteristics (e.g., PF area under CCS, mean and maximum precipitation rate of each PF) and kinematic attributes (e.g., movement speed, movement direction, and centroid position). Additional metrics, such as the size of the cold cloud shield (Tb $<$ 241 K) and the evolution of cloud-top temperature and accumulated precipitation, are recorded at hourly intervals. Together, these variables provide a comprehensive description of MCS structure, intensity, and motion throughout the system lifecycle.

2.3 Precipitation Efficiency Calculation

To calculate MCS ϵ, we first extracted MCS population and lifecycle statistics over the Asian monsoon domain (55°–115°E, 5°S–40°N) during the 2016 monsoon period, which coincides with the peak occurrence of organized convection in the region

https://doi.org/10.5194/egusphere-2026-1395
Preprint. Discussion started: 1 April 2026

(e.g., Virts and Houze, 2016; Paul et al., 2025). A total of 1321 MCSs were identified and tracked by PyFLEXTRKR during this period, which provides a representative sample of monsoon-season MCS activity. This period also corresponds to the DYAMOND Phase I period, so that model evaluation of MCS ϵ could be performed in a subsequent study. To compute ϵ, we collocated ERA5 LWP and IWP fields (summed to yield CWP) in space and time with both the FLEXTRKR pixel-level precipitation fields and the track-level MCS statistics. Specifically, ERA5 fields were bilinearly interpolated to the IMERG grid ($0.1^\circ \times 0.1^\circ$) for the pixel-level calculations, and temporally matched to the nearest IMERG hourly time step. The same temporally matched ERA5 fields were then aggregated to the MCS-track framework to compute ϵ as a function of MCS lifecycle stage. Following Li et al. (2022), ϵ was calculated as:

$$\epsilon = \frac{<\dot{P}>}{<\mathrm{CWP}>} \quad \frac{[\mathrm{kg\ m^{-2}\ h^{-1}}]}{[\mathrm{kg\ m^{-2}}]} \tag{1}$$

where $\dot{P}$ denotes the surface precipitation rate of IMERG and CWP represents the vertically integrated cloud condensate from ERA5. We can calculate ϵ either for instantaneous $\dot{P}$ and CWP over the MCS lifecycle or for time-averaged values from gridded data, as indicated by the brackets in equation (1). Along with ϵ evaluated for total CWP, we also phase-partition values into an ice-phase efficiency, ϵ_i, using IWP and a liquid-phase one, ϵ_ℓ, using LWP.

3 Results

3.1 MCS versus non-MCS precipitation efficiency across the Asian monsoon area

We begin by investigating the distribution of ϵ for individual MCS tracks to characterize the full range of efficiency observed across all systems (Figure 2). When averaged over the lifetime and spatial extent of each MCS track, the ϵ_{cwp} exhibits the lowest median value of $\sim$11.8 $\mathrm{h^{-1}}$, whereas the ice-phase efficiency (ϵ_i) and liquid-phase efficiency (ϵ_ℓ) efficiencies show substantially larger median values that are approximately twice as large (Figure 2a-c). When considering the maximum efficiency attained during each MCS lifecycle, defined as the maximum over the lifetime of the spatially averaged ϵ within the MCS area, the distributions shift toward higher values, with median efficiencies increasing to $\sim$31.8 $\mathrm{h^{-1}}$ for ϵ_{cwp}, $\sim$40.1 $\mathrm{h^{-1}}$ for ϵ_i, and $\sim$43.8 $\mathrm{h^{-1}}$ for ϵ_ℓ (Figure 2d-f). Relative to the lifetime-mean values, these maxima correspond to increases of approximately 170%, 67%, and 85% for ϵ_{cwp}, ϵ_i, and ϵ_ℓ, respectively. Consistent with the shift toward larger values in the distributions, the maximum precipitation efficiency PDFs exhibit positive skewness, indicating that the distributions are characterized by a longer tail toward higher efficiency values. The skewness follows a similar pattern across the three efficiency metrics, with the lifetime-mean efficiencies showing moderate positive skewness, whereas the maximum efficiencies exhibit substantially larger skewness values. This pattern indicates that most MCSs cluster around moderate efficiencies, whereas a small number of systems produce short-lived high-efficiency events that extend the upper tail of the distributions. The larger skewness of the maximum distributions reflects the infrequent occurrence of very high efficiency values during MCS lifecycles, similar to the right-skewed nature commonly observed in precipitation rate distributions.

We then compare the spatial distribution of ϵ for MCS versus non-MCS precipitation (Figure 3). We quantify spatial differences with $\Delta\epsilon$, defined as the difference in MCS versus non-MCS ϵ. Across the region and for both overall and phase-

https://doi.org/10.5194/egusphere-2026-1395
Preprint. Discussion started: 1 April 2026

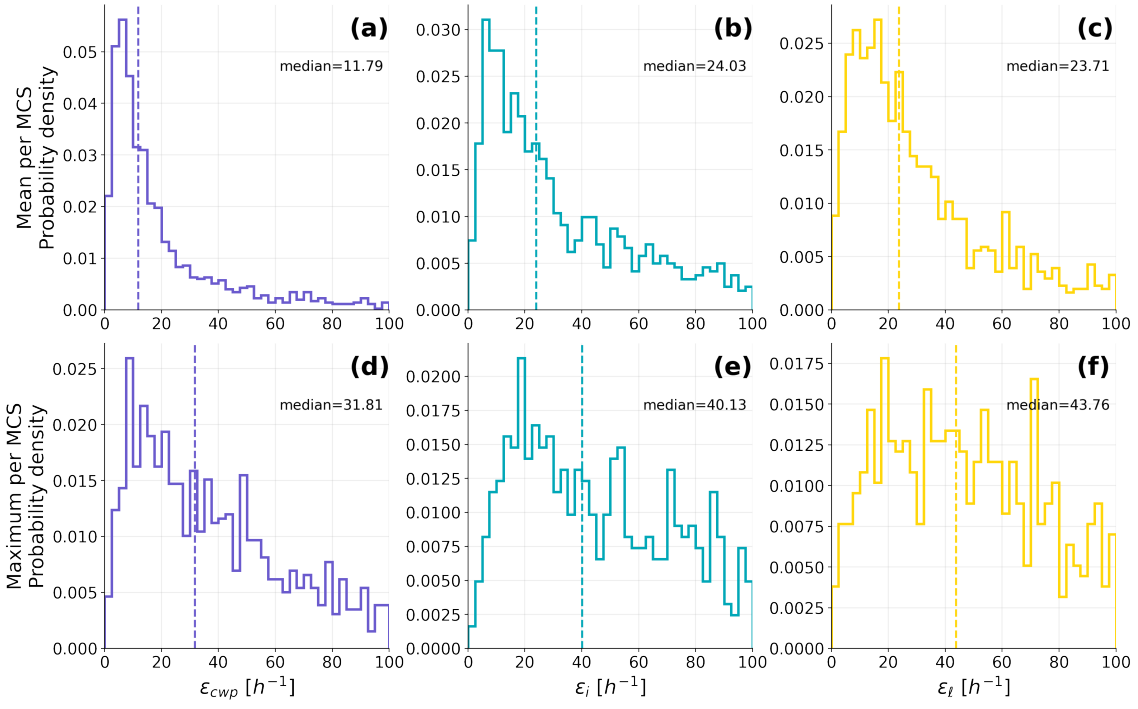

Figure 2. *The median values for ϵ_i and ϵ_ℓ differ by less than 2%, indicating that both condensate phases contribute comparably to precipitation production in MCSs.* Probability density functions (PDFs) of precipitation efficiency (ϵ) across all mesoscale convective systems (MCSs) over the Asian monsoon region. The top row (a–c) shows the distributions of ϵ averaged over the lifetime of each MCS track, while the bottom row (d–f) shows the distributions of the maximum efficiency attained during each MCS lifecycle. The three columns correspond to total efficiencies based on column water path (ϵ_{cwp}), ice-phase efficiency (ϵ_i), and liquid-phase efficiency (ϵ_ℓ), respectively. Dashed vertical lines indicate the median value of each distribution, with values annotated in each panel.

partitioned ϵ, MCSs exhibit values approximately 50% higher than those of non-MCS convection, with the strongest contrasts occurring over the Bay of Bengal, the Indo-Gangetic Plain, and the South China Sea. The MCS ϵ_{cwp} locally exceeds 6 h^{-1}, while that of non-MCS convection typically remains below 3 h^{-1} (Figure 3a and d); these values correspond to condensate lifetimes of approximately 15 and 30 minutes, respectively. The spatial distribution of $\Delta\epsilon_{\mathrm{cwp}}$ further reveals a widespread positive difference greater than 1 h^{-1}, extending from the equatorial Indian Ocean through the Bay of Bengal into the South China Sea regions characterized by frequent occurrence of MCS (Figure 3g). In these areas, MCSs convert condensate to precipitation two to three times more efficiently than non-MCS convection. Interpreted as condensate residence time, these differences imply that hydrometeors typically sediment out within 10 minutes to 1 hour within MCSs, whereas the same condensate can remain aloft for two to four hours before precipitating in non-MCS convection. This substantial reduction in residence time within MCSs reflects their accelerated microphysical processing, driven by ascent within their protected updrafts.

https://doi.org/10.5194/egusphere-2026-1395
Preprint. Discussion started: 1 April 2026

To further elucidate which processes generate $\Delta\epsilon$, we also examine the phase-partitioned efficiencies. The ϵ_i is two- to four-fold larger than the ϵ_ℓ for MCSs (Figure 3b and c). The larger ϵ_i is consistent with efficient ice-phase growth and precipitation formation pathways in deep convection (e.g., deposition, riming, and aggregation), with melting of precipitating ice further contributing to surface rainfall. Additional contributors may include differences in the spatial/vertical distribution of ice versus liquid condensate within MCSs. The same ratio of ϵ_i to ϵ_ℓ characterizes non-MCS. The corresponding non-MCS ϵ_i and ϵ_ℓ are substantially smaller, approximately 50% lower than the MCS equivalents across the domain. Area-weighted mean enhancements over our domain show larger MCS–non MCS contrasts for ϵ_i than for ϵ_ℓ: The domain mean $\Delta\epsilon_i$ is 1.35 h^{-1} versus 1.06 h^{-1} for $\Delta\epsilon_\ell$. The spatial coverage of $\Delta\epsilon$ greater than 0.5 h^{-1} is also 60% for the ice phase and only 52% for the liquid phase (Figure S1). Looking at these phase-partitioned MCS-non MCS differences statistically, across all metrics high ϵ greater than 6 h^{-1} occurs much more frequently in MCSs and particularly for the ice-phase component (Figure S2).

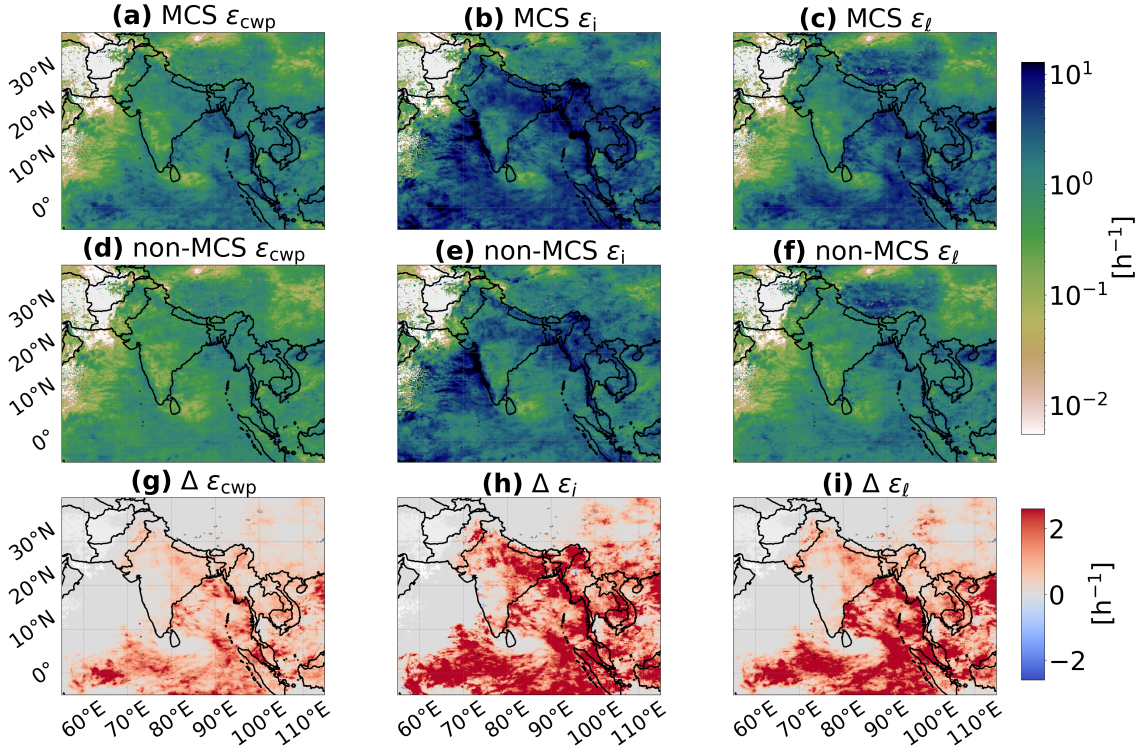

Figure 3. *MCSs exhibit much higher ϵ with mean values 50% greater than for non-MCS convection across all phases.* Spatial distribution of ϵ metrics over the Asian monsoon region for MCSs and non-MCS convection. The top row (a–c) shows MCS ϵ based on overall cloud water path (ϵ_{cwp}), ice water path (ϵ_i), and liquid water path (ϵ_ℓ). The middle row (d–f) presents the corresponding non-MCS precipitation efficiencies, while the bottom row (g–i) shows the MCS-non MCS differences ($\Delta\epsilon = \epsilon^{MCS} - \epsilon^{non\text{-}MCS}$).

https://doi.org/10.5194/egusphere-2026-1395
Preprint. Discussion started: 1 April 2026

3.1.1 Dependence on longitude and latitude

While the spatial maps highlight regions of larger and smaller MCS ϵ, they do not fully reveal how these efficiencies evolve over the west–east monsoon moisture gradient or the north–south land–ocean contrasts. To characterize these variations more explicitly, we evaluate the longitudinal and latitudinal dependence of ϵ_{cwp} and its phase-partitioned values. For each degree longitude, ϵ values represent all grid cells located along that longitude, i.e., '60°E' includes all grid cells along 60°E across the domain latitudes. The same approach is applied for degrees latitude.

Longitudinally, the median ϵ_{cwp} increases steadily from ∼0.2 h^{-1} in the western Arabian Sea around 60°E to a maximum of 1.8 h^{-1} in the eastern Bay of Bengal near 95°E (Figure 4a). The same longitudinal increase is present in ϵ_{cwp} from non-MCS, although these values are lower than the MCS counterparts. This eastward increase in ϵ metrics is consistent with progressively stronger deep convection, greater column moisture availability, warmer sea surface temperatures, and more frequent MCS activity east of 80°E over the Bay of Bengal and the South China Sea. Relative to non-MCS values, MCS ϵ_{cwp} values also have much broader spreads: Indeed, the interquartile range (IQR) of MCS ϵ_{cwp} can be as large as 2.5 h^{-1}, roughly four times larger than that of non-MCS ϵ_{cwp}. This variability indicates that while MCSs are on average more efficient, they also span a wider range of stages and sizes (e.g., developing vs mature vs decaying systems, varying microphysical processes and sizes). Complex terrain further introduces spatial heterogeneity in ϵ metrics by altering condensate residence time. Orographic lifting and flow blocking over complex terrain enhance condensate retention within MCS anvils, leading to non-monotonic longitudinal variations in ϵ and highlighting the role of topography in regulating ϵ (Figure S5). The skewedness of ϵ_{cwp} from MCSs is also much more pronounced than from non-MCSs, with 95th-percentile values as high as 4 h^{-1} (Figure S3). This variability reflects localized convective bursts embedded within larger stratiform outflow regions.

As for the full spatial maps, we next consider the longitudinal gradients in the phase-partitioned ϵ metrics. ϵ_i has the strongest longitudinal variability among the three ϵ metrics (Figure 4c). In the Arabian Sea (60°–70°E) and the Bay of Bengal (85°–95°E), ϵ_i increases eastward, with the 95th percentile often exceeding 8 h^{-1} (Figure S3). Conversely, ϵ_i decreases over the continental region between these two basins, indicating a strong land–ocean contrast. This reduction over land is unique to ϵ_i: It does not appear in ϵ_ℓ and is sufficiently strong that it partially offsets the eastward increase seen in ϵ_{cwp}. Across nearly all longitudes, the IQR of ϵ_i is consistently larger than that of ϵ_{cwp}, increasing by a factor of 3 at certain longitudes (Figure S3). This broader spread indicates greater spatial variability in ϵ_i. Non-MCS ϵ_i remains much lower than the MCS values but exhibits the same decrease over the continental region as for MCSs. This continental reduction is therefore a robust characteristic of the ice phase rather than a feature unique to organized convection.

Latitudinally, ϵ_{cwp} tends to decrease from the equatorial belt northward, consistent with reductions in deep convective intensity and moisture availability further from the tropical convergence zones (Figure 4b). For MCSs, the median ϵ_{cwp} reaches a peak at 2 h^{-1} near the equator and decreases to 1 h^{-1} near 15°N. Between 15° and 20°N, ϵ_{cwp} increases again to 1.4 h^{-1}, as the domain becomes more continental and influenced by orographic forcing from the Himalayan foothills, the Western Ghats, the Arakan Yoma range, and the margins of the Tibetan Plateau. North of 25°N, ϵ_{cwp} drops again to values as low as 0.2 h^{-1}. ϵ_i also shows latitudinal fluctuations in its values with two distinct maxima: one near the equator and a second between

https://doi.org/10.5194/egusphere-2026-1395
Preprint. Discussion started: 1 April 2026

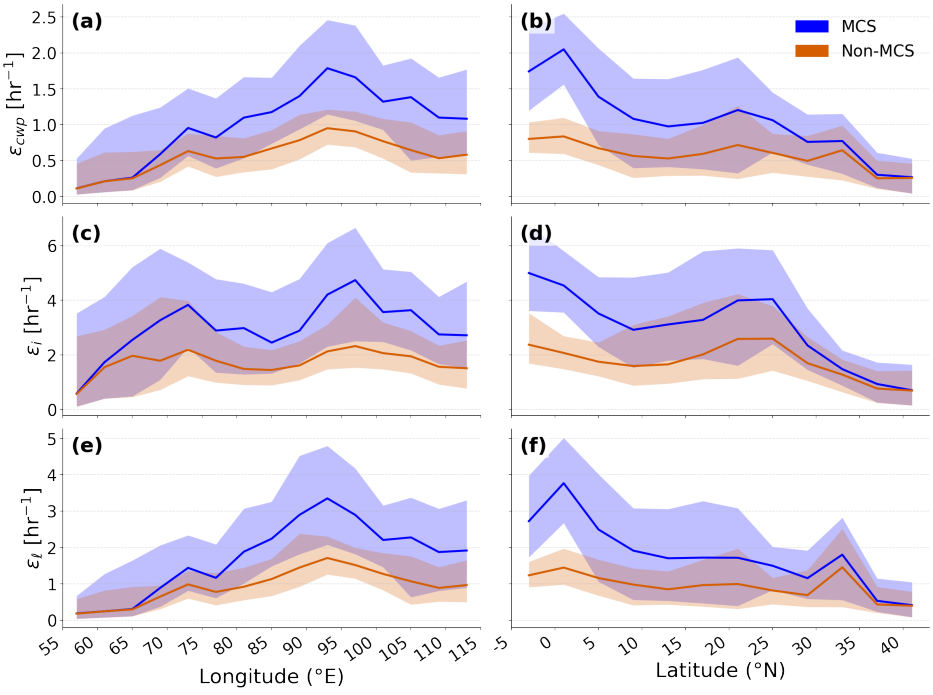

Figure 4. *ϵ tends to increase from west to east and from north to south across our domain, especially in the ice phase.* Longitudinal (left column) and latitudinal (right column) variability of ϵ over the Asian monsoon region for Mesoscale Convective Systems (MCS; blue) and Non-MCS (orange). Rows show (a–b) total precipitation efficiency based on column water path, ϵ_{cwp}, (c–d) ice-phase efficiency, ϵ_i, and (e–f) liquid-phase efficiency, ϵ_ℓ. Solid lines denote the median ϵ within longitude or latitude bins, while shaded envelopes indicate the interquartile range (IQR; 25th–75th percentiles), representing the spread of grid-cell values within each bin

15° and 25°N, corresponding to the monsoon rainband (Figure 4d). As for ϵ_{cwp}, ϵ_i declines sharply northward of 25°N. ϵ_ℓ contains the same general northward decrease as ϵ_{cwp}, although with higher mean values and, hence, shorter residence times for liquid condensate (Figure 4f). These latitudinal fluctuations in ϵ metrics again reflect the land-ocean contrast and impact of topography on MCS condensate and precipitation. Lastly, we point out that the spread of ϵ metrics is again higher for MCS than non-MCS and largest in the ice phase across the latitudes of our domain.

3.1.2 Dependence on precipitation efficiency metric

Before discussing how ϵ metrics change with MCS characteristics, we close this section by examining sensitivity of our spatial results to the definition of ϵ. In Figure 5, we present maps of ϵ using an alternate definition recently reported by Kukulies et al. (2026) in which ϵ is defined as the ratio of surface precipitation to the sum of surface precipitation and the positive tendency of IWP, such that only periods of ice condensate growth are considered:

https://doi.org/10.5194/egusphere-2026-1395
Preprint. Discussion started: 1 April 2026

$$\mathrm{PE} \cong \frac{\dot{P}}{\left(\dot{P} + \left.\frac{\delta \mathrm{IWP}}{\delta t}\right|_{[>0]}\right)} \tag{2}$$

where $\left.\frac{\delta \mathrm{IWP}}{\delta t}\right|_{>0}$ represents the positive tendency of IWP, accounting only for condensate growth and excluding depletion processes such as melting, sublimation, and advection. IWP is used from the CCIC retrieval (see Section 2.1), offering a more observation-based estimate than reanalysis products, where condensate fields depend on microphysical and convective parameterizations. A limitation of this approach is that only the ice phase is considered, implicitly assuming that ice processes dominate precipitation production in deep convective systems. While this formulation differs from Li et al. (2022) in that it defines a dimensionless precipitation efficiency (PE) by relating surface $\dot{P}$ to derived condensation rates, we can nevertheless compare the spatial patterns from both approaches to assess whether the metrics capture the same dominant spatial patterns of condensate-to-precipitation conversion. Despite differences in physical formulation and the different datasets used, the large-scale spatial distributions of ϵ derived using the Li et al. (2022) and Kukulies et al. (2026) definitions are quite similar ($\rho \approx 0.6$, $p \ll 0.01$) across the Asian monsoon region. Similar features, including especially high efficiencies over the Bay of Bengal and Himalayan foothills and especially low efficiencies near the southern tip of India, also appear across the two definitions. This agreement supports the robustness of our spatial analysis and lends confidence to the use of the Li et al. (2022) ϵ definition in this study.

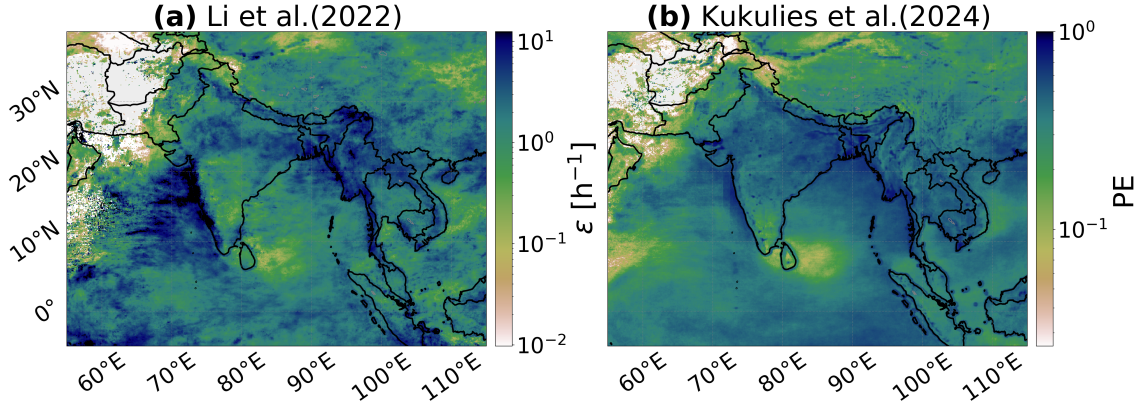

Figure 5. *Similar spatial patterns across two independent ϵ formulations provides confidence in the robustness of our results.* Spatial distribution of ϵ over the Asian monsoon region. (a) Li et al. (2022) ϵ formulation, expressed as an index (h^{-1}), and (b) Kukulies et al. (2026) PE formulation, expressed as a dimensionless fraction bounded between 0 and 1. A statistically significant Spearman rank correlation ($\rho \approx 0.6; p \ll 0.01$) indicates strong spatial similarity between the two formulations.

https://doi.org/10.5194/egusphere-2026-1395
Preprint. Discussion started: 1 April 2026

3.2 Precipitation efficiency across MCS morphologies

Having established the geographic characteristics of MCS versus non-MCS ϵ, we next investigate how ϵ is distributed across regions of the MCS—core, warm anvil, and cold anvil—and across MCSs of different structure. Core clouds correspond to the coldest Tb $\leq$ 225 K. The cold anvil comprises somewhat warmer Tb from 225 K up to 241 K, while the warm anvil represents the warmest cloud-tops from 241 K up to 261 K. Together, these thresholds separate intense convective updrafts from layered anvil outflow in MCSs.

We begin by examining ϵ_{cwp} across the three MCS morphologies. Across all regions, ϵ_{cwp} ranges from 0.1 h^{-1} up to 100 h^{-1}, with the core dominating the high-efficiency tail of the distribution (Figure 6a). These ϵ_{cwp} values correspond to a spread in condensate lifetimes from only a few minutes ($\epsilon_{\mathrm{cwp}} \leq 10$ h^{-1}) up to $\sim$10 hours. The lower ϵ_{cwp} values within the warm and cold anvil regions are reflected in modal values of 3.2 h^{-1} and 1.9 h^{-1}, respectively, compared to 8.4 h^{-1} in the core (Table 1), indicating that anvil efficiencies are approximately 60–80% smaller than core values. Stated in terms of residence time, condensate stays within the anvil three to ten times longer than within the core. This behavior is consistent with strong updrafts, rapid condensate production, and highly efficient ice–liquid conversion within the core of convective towers and weaker ascent and reduced condensate production in the stratiform outflow regions.

We next phase-partition ϵ, both to understand whether the core-cold anvil-warm anvil hierarchy exists in the other ϵ metrics and to determine which phase drives the ϵ differences across MCS morphologies. The core region still contains the highest ϵ_i and ϵ_ℓ; however, the separation in ϵ_i for cold versus warm anvil is less than the separation in ϵ_{cwp} for those regions. The ice phase values shift upward by 30 to 50% relative to ϵ_{cwp}, as established in the previous section. The median of ϵ_i reaches 16.6 h^{-1}, decreasing to 6.9 h^{-1} in the cold anvil and 5.0 h^{-1} in the warm anvil. The difference of ϵ_{cwp} across anvil types is mainly determined by the contribution of ϵ from the liquid phase. This is consistent with recent modeling studies showing that warm-rain and ice-phase pathways coexist in deep convection, and that their relative contributions to precipitation depend on the efficiency of condensate-to-precipitation conversion processes (e.g., autoconversion, riming, aggregation), rather than cloud depth alone (e.g., Gupta et al., 2023). Taken altogether, these distributions of ϵ across MCS morphologies show that the

Table 1. Median values and 95% bootstrap confidence interval(CI) of MCS ϵ metrics, stratified by MCS region (core, cold anvil, and warm anvil) and ice versus liquid phase. The corresponding condensate residence time is shown in minutes.

Metric	MCS morphology	Median values [h^{-1}]	Residence time [min]	CI (low, high) [h^{-1}]
ϵ_{cwp}	Core	8.4	7.1	8.337, 8.379
	Cold Anvil	3.2	18.7	3.228, 3.246
	Warm Anvil	1.9	31.5	1.989, 1.999
ϵ_i	Core	16.4	3.6	16.390, 16.493
	Cold Anvil	6.9	8.6	6.945, 6.995
	Warm Anvil	5.0	12.0	4.995, 5.026
ϵ_ℓ	Core	18.5	3.2	18.499, 18.603
	Cold Anvil	6.4	9.4	6.420, 6.461
	Warm Anvil	3.4	17.6	3.461, 3.483

https://doi.org/10.5194/egusphere-2026-1395
Preprint. Discussion started: 1 April 2026

convective core generates precipitation about four times more efficiently than the warm anvil and two times more efficiently than the cold anvil, with the liquid phase determining much of the ϵ differences across the warm and cold anvil regions.

To understand the difference in warm versus cold anvil ϵ_{cwp}, we visualize the distributions of $\dot{P}$ versus CWP across the MCS morphologies (Figure S4). When min-max normalizing both $\dot{P}$ and CWP, there is greater overlap between these distributions in the warm anvil region than in the cold anvil region. In other words, the difference between condensate amounts aloft and sedimenting is more pronounced in the cold anvil than the warm anvil. Physically, warm anvils are typically characterized by weak vertical velocities, small droplet and ice crystal sizes, and limited microphysical growth via riming, aggregation, or collision–coalescence. Consequently, condensate within warm anvils is predominantly retained in non-precipitating form, resulting in inefficient rainfall production. In contrast, cold anvils, although located at higher altitudes, favor more efficient growth and aggregation of the ice phase, leading to the formation of precipitation-sized hydrometeors that sediment through the melting layer and contribute to stratiform rainfall at the surface. The reduced ϵ_{cwp} of the warm anvils therefore reflects microphysical inefficiency rather than longer residence times, highlighting that the large loading of condensate alone does not imply efficient precipitation production.

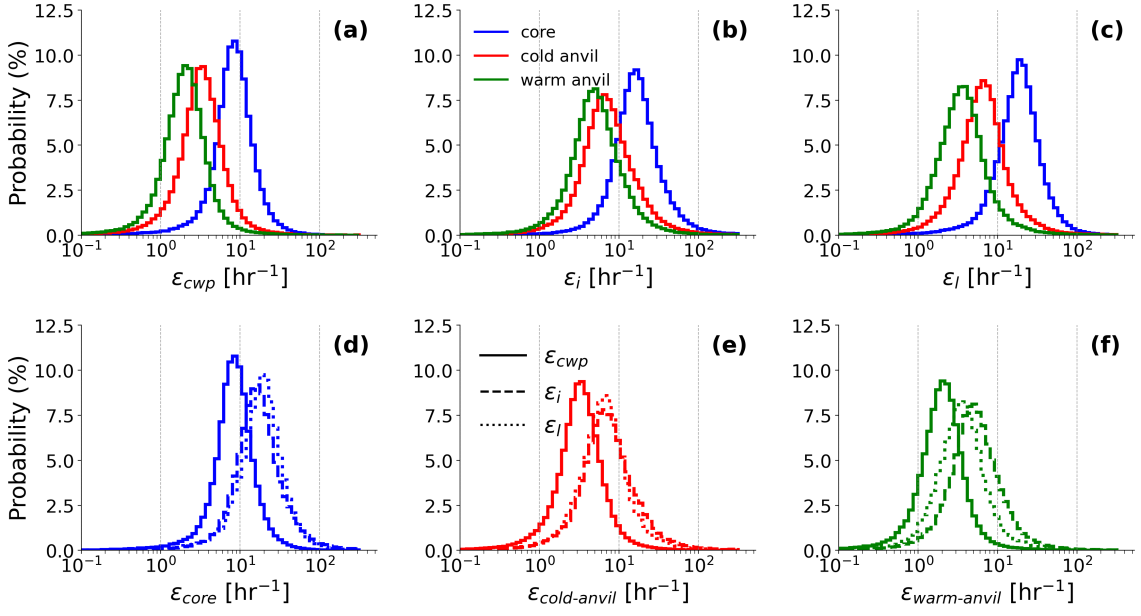

Figure 6. *The core consistently has the highest ϵ values, followed by the cold and then warm anvils, reflecting the transition from deep convective to stratiform and non-precipitating cloud.* Probability distributions of ϵ across MCS morphologies, defined by Tb thresholds in the FLEXTRKR data. Panels (a–c) show distributions of ϵ for the convective core (blue), cold anvil (red), and warm anvil (green) regions, computed for (a) overall precipitation efficiency (ϵ_{cwp}), (b) ice-phase efficiency (ϵ_i), and (c) liquid-phase efficiency (ϵ_ℓ). Panels (d–f) regroup the distributions by MCS region to compare total and phase-partitioned ϵ within each sector: (d) for the core, (e) for the cold anvil, and (f) for the warm anvil. In panels (d–f), solid lines denote ϵ_{cwp}, dashed lines denote ice-phase efficiency (ϵ_i), and dotted lines denote liquid-phase efficiency (ϵ_ℓ).

https://doi.org/10.5194/egusphere-2026-1395
Preprint. Discussion started: 1 April 2026

We lastly reorganize the ϵ distributions by MCS sector to more clearly see the differences across condensate phase (Figure 6d-f). While ϵ_i generally exhibits large values, the relative ordering of ϵ metrics is not consistent across MCS morphologies. Instead, the dominant efficiency shifts from liquid-phase processes in the core to ice-phase processes in the warm anvil, with substantial overlap among metrics in the cold anvil. Rather than indicating a universal hierarchy, these results show that no single microphysical process dominates precipitation production across all MCS morphologies. Instead, the slightly higher ϵ_ℓ in the convective core suggests shorter liquid condensate residence times there, while ϵ_i becomes relatively more prominent in the warm-anvil region. The cold anvil exhibits substantial overlap among phase-partitioned efficiencies, consistent with mixed and intermittent microphysical processes. Together, these patterns suggest that anvils-—particularly their warm portions-—act primarily as regions of condensate storage punctuated by localized, phase-dependent precipitation events.

3.2.1 Dependence on MCS extent and depth

Next, we investigate how ϵ changes with MCS morphology, in particular with the extent and depth of the MCS. MCS area refers to the contiguous cold cloud cover in PyFLEXTRKR (see Section 2.2.1). MCS depth is defined as the vertical extent of the cloud system, inferred from the minimum infrared Tb associated with the convective core and stratiform regions, with colder cloud-top temperatures indicating deeper convection. We stratify our scalings of ϵ versus MCS area and depth by both lifetime mean and maximum rain rates for these systems. All ϵ metrics increase with MCS area for areas less than $\sim 2\times10^4$ km^2 (Figure 7). All three efficiency metrics exhibit statistically significant, strong positive correlations between the mean $\dot{P}$ and MCS area in this range, with r values of 0.98 across the metrics ($p < 10^{-4}$, Figure 7a, Table S1). Among the phase-partitioned ϵ metrics, ϵ_i increases most rapidly with area, reaching a peak value of 30 h^{-1} for an MCS area of 2×10^4 km^2 before decreasing for the largest areas. ϵ_ℓ increases more slowly with MCS area before plateauing at a value of 20 h^{-1} for the largest systems. As a combination of the ice- and liquid-phase scalings, ϵ_{cwp} also increases with MCS area up to a threshold beyond which it declines slightly. This threshold area of 2×10^4 km^2 corresponds to an MCS effective diameter of 160 km. The non-monotonic behavior of the ϵ–area scalings, most pronounced for ϵ_i, likely reflects a disproportionate increase in system-integrated IWP relative to $\dot{P}$ at the largest MCS sizes, such that the accumulation and storage of condensate in extensive stratiform and anvil regions outpaces the corresponding increase in $\dot{P}$.

Scalings of the lifetime maximum $\dot{P}$ against MCS area also increase up to a threshold area but with weaker log-linear correlations (Figure 7b). Correlation coefficients are now 0.95 across the three epsilon metrics but still with statistical significance ($p < 5 \times 10^{-4}$). In contrast to the mean $\dot{P}$ scalings, there is no decrease in ϵ_ℓ beyond a certain MCS area. ϵ_ℓ continues to increase for the largest MCS extents and becomes comparable to or exceeds ϵ_i, indicating that large systems achieve high peak rain rates through both ice and liquid-phase processes. These scalings demonstrate that MCS area strongly controls ϵ, with larger MCSs more efficiently converting cloud condensate into precipitation but only up to a certain point.

We next examine the sensitivity of the ϵ metrics to the MCS depth across mean and max rain rates (Figure 8). ϵ_{cwp}, ϵ_ℓ, and ϵ_i increase systematically with MCS depth, which corresponds to a decreasing Tb. In other words, deeper MCSs more efficiently convert cloud condensate into surface precipitation. The correlation coefficient for these scalings reaches -0.97 across all ϵ metrics with greater than 99% statistical significance, indicating that more than 95% of the variance in ϵ can be

https://doi.org/10.5194/egusphere-2026-1395
Preprint. Discussion started: 1 April 2026

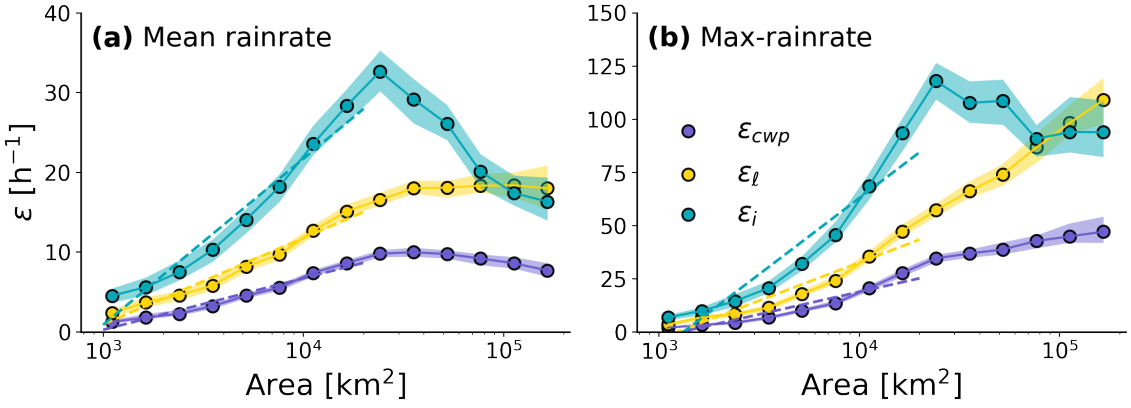

Figure 7. *For both mean and maximum rain rates, ϵ increases with MCS size for areas less than 2×10^4 km^2.* Scalings of the ϵ metrics versus MCS area for (a) lifetime mean rain rate and (b) lifetime maximum rain rate. Curves show the total precipitation efficiency (ϵ_{cwp}, purple), liquid-phase efficiency (ϵ_{ℓ}, yellow), and ice-phase efficiency (ϵ_i, cyan). Dashed lines indicate log–linear fits to the ϵ–area relationship, computed only for MCS areas smaller than 2×10^4 km^2. Shading indicates the 95% bootstrap confidence interval on the binned median ϵ metrics within each MCS-area bin.

explained by variations in the MCS cloud-top temperature (Table S2). ϵ_i increases by more than 150% between the warmest and coldest Tb (Figure 8a). ϵ_{ℓ} also doubles across the Tb range. As for extent, we also scale the maximum $\dot{P}$ against MCS depth. The correlation between the ϵ metrics and Tb remains quite robust with statistically significant coefficients of -0.99 ($p < 10^{-5}$). These near-perfect correlations indicate that the intensity of the maximum rainfall is tightly coupled with the vertical development of the MCSs. ϵ_i is consistently most sensitive to Tb; however, there is no decrease in ϵ_i for the deepest MCSs as there was for the largest MCSs. Unlike the ϵ–area scalings, ϵ metrics does not show the non-monotonic behavior with increasing MCS depth. Increases in ϵ metrics with depth primarily reflect dynamical intensification (e.g., stronger updrafts driven by larger CAPE or reduced entrainment) rather than a requisite increase in total condensate. Because deeper systems do not necessarily accumulate condensate aloft, the ϵ metrics do not decrease at the largest depths. The contrast between these scalings highlights distinct controls on ϵ metrics associated with horizontal versus vertical MCS growth.

3.3 Precipitation efficiency over the MCS lifecycle

We next look at the evolution of ϵ metrics over the MCS lifecycle. The MCS lifecycle is normalized by rescaling the system lifetimes to a common 0–1 interval, where 0 and 1 correspond to initiation and dissipation according to the FLEXTRKR tracking, respectively. All three efficiency metrics show a lifecycle dependence with rapid increases during the early growth stage and more gradual decreases during development and dissipation (Figure 9). Increases in ϵ metrics occur within the first 20% of the lifecycle, while the decreases occur over the remaining 80% during the decay-phase behavior of condensate production (Kukulies et al., 2026). This evolution closely resembles the MCS ϵ lifecycle reported by Kukulies et al. (2026) (their Figure 4b), who found increasing efficiency from initiation to maturity followed by decreasing efficiency from maturity

https://doi.org/10.5194/egusphere-2026-1395
Preprint. Discussion started: 1 April 2026

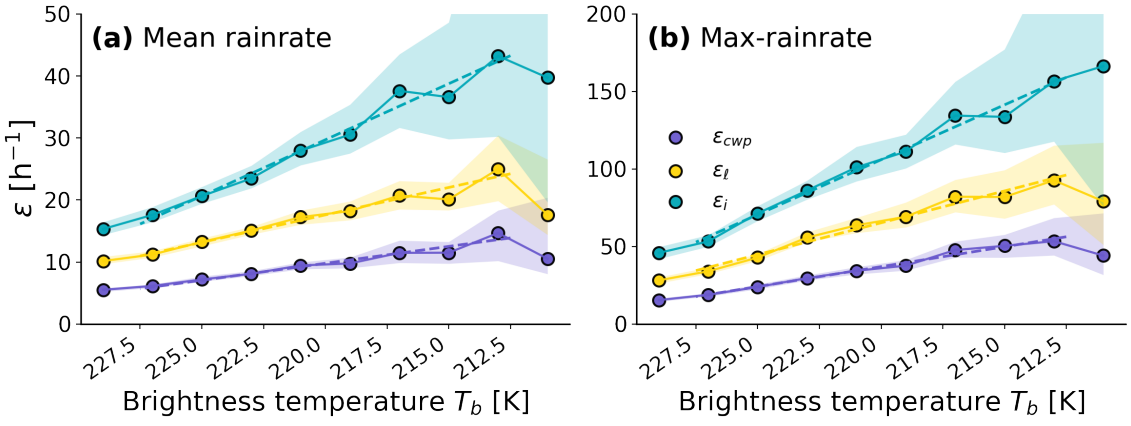

Figure 8. *For both mean and maximum rain rates, ϵ increases as brightness temperature decreases, indicating that deeper convection more effectively converts condensate to rainfall.* Scalings of the ϵ metrics versus cloud-top brightness temperature for (a) lifetime mean rain rate and (b) lifetime maximum rain rate. Curves show the total efficiency (ϵ_{cwp}, purple), liquid-phase efficiency (ϵ_ℓ, yellow), and ice-phase efficiency (ϵ_i, cyan). Dashed lines indicate log–linear fits to the ϵ–depth relationship, and shading indicates the 95% bootstrap confidence interval on the binned median ϵ metrics within each Tb bin.

through decay in kilometer-scale simulations and satellite-based estimates. In our observations, peak ϵ occurs slightly earlier in the normalized lifecycle than in Kukulies et al. (2026). However, the qualitative agreement is notable, despite differences in region and methodology: both studies indicate that MCSs achieve their highest ϵ after convective organization is established, rather than during initial development.

Phase partitioning further refines this evaluation over the lifecycle. The high values of ϵ_i throughout most of the lifecycle align with a central role for ice-phase growth and sedimentation in sustaining efficient rainfall during mature MCS stages. Apart from the hierarchy of magnitudes, the lifecycle behavior of ϵ is quite consistent across all metrics, indicating that phase partitioning plays a secondary role in controlling variations of ϵ over the lifecycle.

This evolution of ϵ over the lifecycle is consistent with our scalings in the previous section, as MCS growth and maturation are characterized by expanding system coverage and progressively colder cloud tops, both of which are associated with enhanced ϵ. In contrast, the late-stage decline in all efficiency metrics coincides with a shrinking system area and a warming of the cloud tops, indicating reduced vertical depth, weaker dynamical organization, and diminished microphysical conversion efficiency. Together, these results demonstrate that the observed lifecycle modulation of ϵ reflects the coupled evolution of storm size, cloud-top height, and microphysics, with ice-phase processes playing a dominant role during periods of maximum system extent and minimum cloud-top temperature.

https://doi.org/10.5194/egusphere-2026-1395
Preprint. Discussion started: 1 April 2026

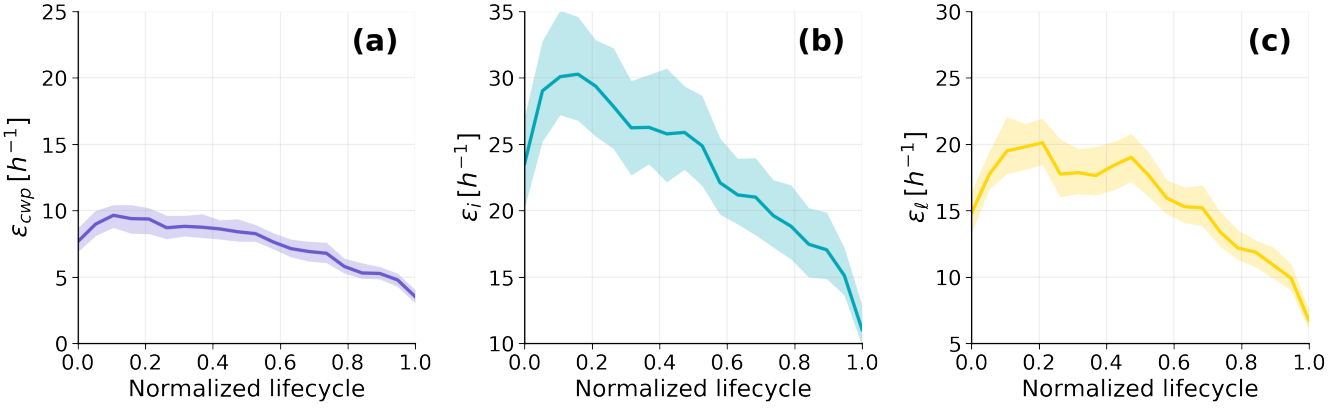

Figure 9. *The ϵ metrics peak within the first 20% of MCS lifecycle.* ϵ metrics computed as a function of normalized MCS lifetime, where 0 indicates system initiation and 1 indicates system dissipation, for (a) ϵ_{cwp}, (b) ϵ_i, and (c) ϵ_ℓ. Each curve represents the average ϵ across all tracked MCSs, and shading represents the 95% bootstrap confidence interval on the median ϵ metrics across MCS tracks at each normalized lifecycle phase. Note that y-axis limits change between panels but have a consistent range of 25 h^{-1}.

4 Conclusions

Accurately representing precipitation associated with mesoscale convective systems (MCSs) remains a major challenge for climate models. Our recent evaluations of DYAMOND storm-resolving simulations against GPM IMERG observations over a South Asian domain show that the largest model–observation precipitation differences occur in regions dominated by frequent MCS activity, including the southern Indian Ocean and the Bay of Bengal (Makgoale and Sullivan, 2025). In these regions, rainfall is primarily produced by organized deep convective systems in which surface precipitation ($\dot{P}$) is strongly regulated by storm morphology, lifecycle, and microphysical processes, meaning that modeled precipitation rates are particularly sensitive to deficiencies in MCS representation. Motivated by these findings, this study provides a comprehensive observational assessment of the efficiency of precipitation production (ϵ) in MCSs over the Asian Monsoon Region. We analyze PyFLEXTRKR MCS track statistics and pixel-level diagnostics in combination with ERA5 cloud condensate fields to characterize ϵ of 1321 MCSs over the Asian monsoon region from 10 August to 10 September 2016 using the Li et al. (2022) index, defined as the ratio of $\dot{P}$ to CWP. We note that ERA5 condensate fields are derived from a data-assimilating forecast model and therefore depend on model microphysical parameterizations. As such, uncertainties in condensate partitioning and phase representation may influence ϵ estimates.

Our results show that for both overall efficiency (ϵ_{cwp}) and ice and liquid phase-partitioned efficiencies (ϵ_i and ϵ_ℓ) MCSs convert cloud condensate into surface precipitation about 50% more efficiently than non-MCS convection. Spatial distributions in the ϵ metrics across the Asian monsoon region further indicate enhanced efficiency in moisture-rich, dynamically favorable environments and reduced efficiency in regions characterized by limited moisture supply, weaker convective organization, or continental interiors. Strong enhancements in MCS ϵ also occur along the Himalayan foothills. Phase-partitioned analyses

https://doi.org/10.5194/egusphere-2026-1395
Preprint. Discussion started: 1 April 2026

reveal that ϵ_i systematically exceeds ϵ_ℓ in both MCS and non-MCS regimes and drives more of the MCS versus non-MCS differences. In contrast, lifecycle evolution in ϵ—characterized by a rapid increase during early growth and more gradual decreases during development and dissipation—is largely phase independent. The decline in ϵ during dissipation stages reflects continued condensate storage within stratiform and anvil regions while surface precipitation weakens.

Another key result of this study is the systematic variation of ϵ across MCS regions from the core to the cold and warm anvils. Decomposing ϵ by MCS region shows that the convective core consistently has the highest efficiency across all ϵ metrics, corresponding to short condensate residence times on the order of a few minutes, whereas warm anvils display the lowest efficiencies, with condensate retained for several hours before contributing to surface precipitation. Efficiency differences between cold and warm anvils are driven by differences in liquid-phase condensate more than by those in the ice phase. Scaling ϵ by MCS area and depth further clarifies the factors controlling rainfall production. The non-monotonic relationships between ϵ and MCS area reflect the disproportionate growth of system-integrated ice condensate associated with anvil expansion in the largest systems, such that condensate accumulation outpaces increases in surface precipitation. In contrast, ϵ increases monotonically with MCS depth, consistent with depth increases being driven primarily by dynamical intensification (e.g., stronger updrafts or reduced entrainment) rather than excess condensate storage. This distinction highlights fundamentally different roles of horizontal and vertical storm growth in regulating ϵ.

Recent work indicates that estimates of storm frequency, size, and duration can vary substantially across tracking methodologies (e.g., Prein et al., 2024; Feng et al., 2025). It would be worthwhile to examine how our results change when using other MCS tracking datasets. As noted in the introduction, many definitions of ϵ exist. We have tested robustness of our spatial analyses to a different PE definition; however, other metrics using microphysical tendencies or moisture convergence could also be tested to compare MCS and non-MCS convection. An important next step is to apply the phase-specific ϵ diagnostics developed here—including morphology-dependent ϵ, residence time estimates, and phase-resolved condensate–precipitation relationships—to storm-resolving model output. This framework enables direct comparison between observed and simulated MCS ϵ, allowing identification of biases in condensate partitioning, conversion rates, and their dependence on system morphology and lifecycle stage. Such a comparison would provide a rigorous benchmark to evaluate how high-resolution models reproduce the structural, microphysical, and lifecycle-dependent characteristics of MCS ϵ identified here. In addition, future studies should examine the seasonal dependence of ϵ, both for MCSs and non-MCS convection, as well as its sensitivity to large-scale environmental conditions, including moisture availability, vertical wind shear, and thermodynamic stability. Addressing these aspects will further clarify the physical controls in ϵ and improve its utility as a diagnostic for model evaluation and climate applications.

Data availability. The GPM IMERG precipitation data are publicly available from the NASA Goddard Earth Sciences Data and Information Services Center (GES DISC; https://disc.gsfc.nasa.gov/datasets/GPM_3IMERGHH_07/summary; Huffman et al. 2023). The CCIC data set is described and validated by Amell et al. (2023) and Pfreundschuh et al. (2025) and is publicly available through Amazon Web Services (CCI, 2026). ERA5 reanalysis data are produced by the European Centre for Medium-Range Weather Forecasts (ECMWF) and can be accessed

https://doi.org/10.5194/egusphere-2026-1395
Preprint. Discussion started: 1 April 2026

through the Copernicus Climate Data Store (CDS; https://cds.climate.copernicus.eu/datasets/reanalysis-era5-single-levels?tab=overview; (Hersbach et al., 2020)). Mesoscale convective system (MCS) tracking in this study was performed using the PyFLEXTRKR tracking framework, and the resulting tracking outputs used in this analysis are available from Dr. Zhe Feng upon request.

Code and data availability. The dataset supporting this study is archived in Zenodo (Makgoale et al., 2026). This archive contains the processed data used to calculate precipitation efficiency of mesoscale convective systems across the Asian Monsoon Region. All Python scripts used to process the data and generate the figures in this study are publicly available at https://github.com/temakgoale/MCS-Precipitation-Efficiency.

Author contributions. T.M. designed the study, performed the data analysis, and led the writing of the manuscript. S.S. supervised the research, contributed to the study design, analysis methodology, and provided scientific guidance and editorial feedback throughout the manuscript development. J.K. contributed to scientific discussions, interpretation of the results, and manuscript revisions. All authors reviewed and approved the final manuscript.

Competing interests. The authors declare that no competing interests are present.

Acknowledgements. This work was supported by the NASA Future Investigators in NASA Earth and Space Science and Technology (FINESST) program under award 23-EARTH23-0019. The authors thank Dr. Zhe Feng for providing the FLEXTRKR dataset used to identify and track mesoscale convective systems (MCSs) and for technical guidance. We acknowledge valuable scientific discussions with Dr. Julia Kukulies and colleagues at the Department of Chemical Engineering, University of Arizona. ERA5 reanalysis data were obtained from the European Centre for Medium-Range Weather Forecasts (ECMWF) under license.

https://doi.org/10.5194/egusphere-2026-1395
Preprint. Discussion started: 1 April 2026

References

Chalmers Cloud Ice Climatology (CCIC) [Dataset], AWS. Retrieved from, https://doi.org/https://registry.opendata.aws/ccic/, 2026.

Amell, A., Pfreundschuh, S., and Eriksson, P.: The Chalmers Cloud Ice Climatology: Retrieval implementation and validation, EGUsphere [preprint], https://doi.org/https://doi.org/10.5194/egusphere-2023-1953, 2023.

Bao, J. and Sherwood, S. C.: The role of convective self-aggregation in extreme instantaneous versus daily precipitation, J. Adv. Model. Earth Syst., 11, 19–33, https://doi.org/https://doi.org/10.1029/2018MS001503, 2019.

Becker, T., Bechtold, P., and Sandu, I.: Characteristics of convective precipitation over tropical Africa in storm-resolving global simulation, Q. J. Roy. Meteorol. Soc., 147, 4388–4407, https://doi.org/10.1002/qj.4185, 2021.

Da-Silva, N. A., Muller, C., Shamekh, S., and Fildier, B.: Significant amplification of instantaneous extreme precipitation with convective self-aggregation, J. Adv. Model. Earth Syst., 13, e2021MS002 607, https://doi.org/https://doi.org/10.1029/2021MS002607, 2021.

Dong, W., Zhao, M., Ming, Y., Krasting, J. P., and Ramaswamy, V.: Simulation of United States Mesoscale Convective Systems using GFDL's New High-Resolution General Circulation Model, Journal of Climate, 36, 6967–6990, https://doi.org/https://doi.org/10.1175/JCLI-D-22-0529.1, 2023.

Doswell, C. A., Brooks, H. E., and Maddox, R. A.: Flash Flood Forecasting: An Ingredients Based Methodology, Weather Forecast., 11, 560–581, https://doi.org/https://doi.org/10.1175/1520-0434(1996)011<0560:FFFAIB>2.0.CO;2, 1996.

Feng, Z., Leung, L. R., Hauze, R. A., Hagos, S., Hardin, J., Yang, Q., Han, and Fan, J.: Structure and Evolution of Mesoscale Convective Systems: Sensitivity to Cloud Microphysics in Convection-Permitting Simulations Over the United States, J. Adv. Model. Earth Sys, 10, 1470–1494, https://doi.org/https://doi.org/10.1029/2018MS001305, 2018.

Feng, Z., Leung, L. R., Liu, N., Wang, J., Houze, R. A., Li, J., Hardin, J. C., Chen, D., and Guo, J.: A Global High-Resolution Mesoscale Convective System Database Using Satellite-Derived Cloud Tops, Surface Precipitation, and Tracking, J. Geophys. Res. Atm., 126, e2020JD034 202, 2021a.

Feng, Z., Song, F., Sakaguchi, K., and Leung, L. R.: Evaluation of Mesoscale Convective Systems in Climate Simulations: Methodological Development and Results from MPAS-CAM over the United States, Journal of Climate, 34, 2611–2633, https://doi.org/https://doi.org/10.1175/JCLI-D-20-0136.1, 2021b.

Feng, Z., Prein, A. F., Kukulies, J. Fiolleau, T., Jones, W. K., and Maybee, B, e. a.: Mesoscale convective systems tracking method inter-comparison (MCSMIP): Application to DYAMOND global km-scale simulations, Journal of Geophysical Research: Atmospheres, 130, e2024JD042 204, https://doi.org/https://doi.org/10.1029/2024JD042204, 2025.

Gupta, A. K., Deshmukh, A., Waman, D., Patade, S., Jadav, A., Phillips, V. T. J., Bansemer, A., Martins, J. A., and Gonçalves, F. L. T.: The microphysics of the warm-rain and ice crystal processes of precipitation in simulated continental convective storms, COMMUNICATIONS EARTH & ENVIRONMENT, 4, https://doi.org/https://doi.org/10.1038/s43247-023-00884-5, 2023.

Han, J.-Y. and Hong, S.-Y.: Precipitation forecast experiments using the Weather Research and Forecasting (WRF) model at gray-zone resolutions, Weather Forecast., 33, 1605–1616, https://doi.org/10.1175/WAF-D-18-0026.1., 2018.

Hernández, K. S., Henao, J. J., Gómez-Ríos, S., Robledo, V., Rendón, A. M., and Mejía, J. F.: Spatio-Temporal Representation of Mesoscale Convective Systems in Convection-Permitting Simulations Over Northwestern South America: Insights Into Rainfall Overestimation, Journal of Geophysical Research: Atmospheres, 130, e2024JD042 289, https://doi.org/https://doi.org/10.1029/2024JD042289, 2025.

Hersbach, H., Bell, B., Berrisford, P., Hirahara, S., Horányi, A., noz-Sabater, J. M., Nicolas, J., Peubey, C., Radu, R., Schepers, D., Simmons, A., Soci, C., Abdalla, S., Abellan, X., Balsamo, G., Bechtold, P., Biavati, G., Bidlot, J., Bonavita, M., Chiara, G. D., Dahlgren, P., Dee,

https://doi.org/10.5194/egusphere-2026-1395
Preprint. Discussion started: 1 April 2026

D., Diamantakis, M., Dragani, R., Flemming, J., Forbes, R., Fuentes, M., Geer, A., Haimberger, L., Healy, S., Hogan, R. J., Hólm, E., Janisková, M., Keeley, S., Laloyaux, P., Lopez, P., Lupu, C., Radnoti, G., de Rosnay, P., Rozum, I., Vamborg, F., Villaume, S., and Thépautet, J.: The ERA5 global reanalysis, Q. J. Roy. Meteorol. Soc., 146, 1999–2049, 2020.

Houze, Robert. A., J.: Mesoscale convective systems, Rev. Geophys., 42, RG4003, https://doi.org/doi:10.1029/2004RG000150, 2004.

Hsu, W. C., Kooperman, G. J., Hannah, W. M., Reed, K. A., Akinsanola, A. A., and Pendergrass, A. G.: Evaluating Mesoscale Convective Systems Over the US in Conventional and Multiscale Modeling Framework Configurations of E3SMv1, Journal of Geophysical Research: Atmospheres, 128, e2023JD038 740, https://doi.org/https://doi.org/10.1029/2023JD038740, 2023.

Huffman, G. J., Bolvin, D. T., Braithwaite, D., Hsu, K., Joyce, R., Kidd, C., Nelkin, E. J., Sorooshian, S., Tan, J., and Xie, P.: NASA Global Precipitation Measurement (GPM) Integrated Multi-satellitE Retrievals for GPM (IMERG), Algorithm Theoretical Basis Doc., 6, 38pp, https://doi.org/https://gpm.nasa.gov/sites/default/files/document_files/IMERG_ATBD_V06_0.pdf, 2019a.

Huffman, G. J., Stocker, E. F., Bolvin, D., Nelkin, E., and Tan, J.: GPM IMERG Final Precipitation L3 Half Hourly 0.1 degree x 0.1 degree V07, Greenbelt, MD, Goddard Earth Sciences Data and Information Services Center (GES DISC), Accessed, https://doi.org/10.5067/GPM/IMERG/3B-HH/07, 2023.

Janowiak, J., Joyce, J., and Xie, P.: NCEP/CPC L3 Half Hourly 4km Global (60S - 60N) Merged IR V1, Edited by Andrey Savtchenko, Greenbelt, MD, Goddard Earth Sciences Data and Information Services Center (GES DISC), https://doi.org/https://doi.org/10.5067/P4HZB9N27EKU, 2017.

Judt, F. and Rios-Berrios, R.: Resolved convection improves the representation of equatorial waves and tropical rainfall variability in a global nonhydrostatic model., Geophysical Research Letters, 48, e2021GL093 265, https://doi.org/https://doi.org/10.1029/2021GL093265, 2021.

Kukulies, J., Prein, A. F., Done, J., Stansfield, A. M., and Berrios, R. R.-.: Precipitation Efficiency by Storm Type in Km-scale Climate Simulations and Satellite Observations, Journal of Geophysical Research: Atmospheres, 131, e2025JD044 800, https://doi.org/https://doi.org/10.1029/2025JD044800, 2026.

Li, R. L., Studholme, J. H. P., Fedorov, A. V., and Storelvmo, T.: Precipitation efficiency constraint on climate change, Nature Climate Change, 12, 642–648, 2022.

Lin, G., Jones, C. R., Leung, L. R., Feng, Z., and Ovchinnikov, M.: Mesoscale Convective Systems in a Superparameterized E3SM Simulation at High Resolution, Journal of Advances in Modeling Earth Systems, 14, e2021MS002 660, https://doi.org/https://doi.org/10.1029/2021MS002660, 2022.

Liu, C.: Rainfall Contributions from Precipitation Systems with Different Sizes, Convective Intensities, and Durations over the Tropics and Subtropics, J. Hydrometeor., 12, 394–412, https://doi.org/https://doi.org/10.1175/2010JHM1320.1, 2012.

Lutsko, N. J. and Cronin, T. W.: Increase in Precipitation Efficiency With Surface Warming in Radiative Convective Equilibrium, Journal of Advances in Modeling Earth Systems, 10, 2990–3010, https://doi.org/https://doi.org/10.1029/2018MS001482, 2018.

Ma, H. Y., Klein, S. A., Lee, J., Ahn, M. S., Tao, C., and Gleckler, P. J.: Superior daily and sub-daily precipitation statistics for intense and long-lived storms in global storm-resolving models, Geophysical Research Letters, 49, e2021GL096 759, https://doi.org/https://doi.org/10.1029/2021GL096759, 2022.

Makgoale, T. E. and Sullivan, S. C.: Characterization and comparison of simulated precipitation efficiency from global storm-resolving models over the Asian monsoon region, Journal of Geophysical Research: Atmospheres, 130, e2025JD044 228, https://doi.org/https://doi.org/10.1029/2025JD044228, 2025.

https://doi.org/10.5194/egusphere-2026-1395
Preprint. Discussion started: 1 April 2026

Makgoale, T. E., Sullivan, S. C., and Kukulies, J.: Dataset for: An Observational Perspective on Precipitation Efficiency of Mesoscale Convective Systems over the Asian Monsoon Region (v1.0) [Data set]., Zenodo, https://doi.org/https://doi.org/10.5281/zenodo.19350427, 2026.

Mauritsen, T. and Stevens, B.: Missing iris effect as a possible cause of muted hydrological change and high climate sensitivity in models, Nature Geoscience, 8, 346–351, https://doi.org/https://doi.org/10.1038/ngeo2414, 2015.

Na, Y., Fu, Q., and Kodama, C.: Precipitation Probability and Its Future Changes From a Global Cloud-Resolving Model and CMIP6 Simulations, Journal of Geophysical Research: Atmospheres, 125, e2019JD03 192, https://doi.org/https://doi.org/10.1029/2019JD031926, 2020.

Paul, K., Dubey, S., and Cui, W.: Mesoscale Convective Systems over South Asia: Unraveling climatology, land-ocean differences and environmental drivers, Climate Dynamics, 63, https://doi.org/https://doi.org/10.1007/s00382-025-07844-z, 2025.

Pfreundschuh, S., Kukulies, J., Amell, A., Hallborn, H., May, E., and Eriksson, P.: The Chalmers Cloud Ice Climatology: A Novel Robust Climate Record of Frozen Cloud Hydrometeor Concentrations, Journal of Geophysical Research: Atmospheres, 130, e2024JD042 618, https://doi.org/https://doi.org/10.1029/2024JD042618, 2025.

Prein, A. F., Feng, Z., Fiolleau, T., Moon, Z. L., Ocasio, K. M. N., Kukulies, J., Roca, R., Varble, A. C., Rehbein, A., Liu, C., Ikeda, K., Mu, Y., and Rasmussen, R. M.: Km-scale simulations of mesoscale convective systems over South America—A feature tracker intercomparison, Journal of Geophysical Research: Atmospheres, 129, e2023JD040 254, https://doi.org/https://doi.org/10.1029/2023JD040254, 2024.

Song, J., Song, F., Feng, Z., Leung, L. R., Li, C., and Wu, L.: Realistic Precipitation Diurnal Cycle in Global Convection-Permitting Models by Resolving Mesoscale Convective Systems, Geophysical Research Letters, 51, e2024GL109 945, https://doi.org/https://doi.org/10.1029/2024GL109945, 2024.

Stevens, B.: On the Growth of Layers of Nonprecipitating Cumulus Convection, J. Atm. Sci., 64, 2916–2931, https://doi.org/https://doi.org/10.1175/JAS3983.1, 2007.

Stevens, B., Satoh, M., Auger, L., Biercamp, J., Bretherton, C. S., Chen, X., Duben, P., Judt, F., Khairoutdinov, M., Klocke, D., Kodoma, C., Kornblueh, L., Lin, S. J., Neumann, P., Putman, W. M., Rober, N., Shibuya, R.and Vanniere, B., Vidale, P. L., Wedi, N., and Zhou, L.: DYAMOND: The dynamics of the atmospheric general circulation modeled on non-hydrostatic domains, Progress in Earth and Planetary Science, 6, 61, https://doi.org/https://doi.org/10.1186/s40645-019-0304-z, 2019.

Sui, C. H., Satoh, M., and Suzuki, K.: Precipitation Efficiency and its Role in Cloud-Radiative Feedbacks to Climate Variabili, Journal of the Meteorological Society, 98, 261–282, https://doi.org/doi:10.2151/jmsj.2020-024, 2020.

Tao, W.-K., Johnson, D., Shie, C.-L., and Simpson, J.: The Atmospheric Energy Budget and Large-Scale Precipitation Efficiency of Convective Systems during TOGA COARE, GATE, SCSMEX, and ARM: Cloud-Resolving Model Simulations, J. Atm. Sci., 61, 2405–2423, https://doi.org/https://doi.org/10.1175/1520-0469(2004)061<2405:TAEBAL>2.0.CO;2, 2004.

Virts, K. S. and Houze, R. A.: Seasonal and Intraseasonal Variability of Mesoscale Convective Systems over the South Asian Monsoon Region, Journal of the Atmospheric Sciences, 73, 4753–4773, https://doi.org/10.1175/JAS-D-16-0022.1, 2016.

Wing, A. A., Emanuel, K., Holloway, C. E., and Muller, C.: Convective Self-Aggregation in Numerical Simulations: A Review, Surv. Geophys., https://doi.org/DOI 10.1007/s10712-017-9408-4, 2017.

Zhang, Z., Varble, A., Feng, Z., Hardin, J., and Zipser, E.: Growth of Mesoscale Convective Systems in Observations and a Seasonal Convection-Permitting Simulation over Argentina, Mon. Weather Rev., 149, 3469—-3490, 2021.